Titre: Title:	Refractory plasmonics of reactively sputtered hafnium nitride nanoparticles : pushing limits
Auteurs: Authors:	Pavel Pleskunov, Mariia Protsak, Zdeněk Krtouš, Tereza Košutová, Marco Tosca, Kateryna Biliak, Veronika Cervenková, Daniil Nikitin, Jan Hanuš, Miroslav Cieslar, Ivan Gordeev, Milan Dopita, Michael Vorochta, Jaroslav Kousal, Ludvik Martinu, & Andrei Choukourov
Date:	2024
Type:	Article de revue / Article
Référence: Citation:	Pleskunov, P., Protsak, M., Krtouš, Z., Košutová, T., Tosca, M., Biliak, K., Cervenková, V., Nikitin, D., Hanuš, J., Cieslar, M., Gordeev, I., Dopita, M., Vorochta, M., Kousal, J., Martinu, L., & Choukourov, A. (2024). Refractory plasmonics of reactively sputtered hafnium nitride nanoparticles : pushing limits. Advanced Optical Materials, 12(13), 202302715 (13 pages). https://doi.org/10.1002/adom.202302715

Document en libre accès dans PolyPublie
Open Access document in PolyPublie

Document publié chez l'éditeur officiel
Document issued by the official publisher

Refractory Plasmonics of Reactively Sputtered Hafnium Nitride Nanoparticles: Pushing Limits

Pavel Pleskunov,* Mariia Protsak, Zdeněk Krtouš, Tereza Košutová, Marco Tosca, Kateryna Biliak, Veronika Červenková, Daniil Nikitin, Jan Hanuš, Miroslav Cieslar, Ivan Gordeev, Milan Dopita, Michael Vorochta, Jaroslav Kousal, Ludvik Martinu, and Andrei Choukourov*

High-temperature plasmonics deals with optically active nanostructures that can withstand high temperatures. A conventional approach relying on standalone noble metal nanoparticles fails to deliver refractory plasmonic nanomaterials, and an alternative route envisions metal nitrides. The main challenge remains the development of advanced synthesis techniques and the insight into thermal stability under real-life application conditions. Here, hafnium nitride nanoparticles (HfN NPs) can be produced by gas aggregation using reactive magnetron sputtering, a technique with a small environmental footprint are shown. As-deposited NPs are of 10 nm mean size and consist of stoichiometric, crystalline *fcc* HfN. They are characterized by optical absorption below 500 nm caused by interband transitions and in the red/near-infrared (NIR) region due to intraband transitions and localized surface plasmon resonance (LSPR). The optical response can be engineered by tuning the NP composition as predicted by finite-difference time-domain (FDTD) calculations. Going beyond the state-of-the-art, the HfN NP thermal stability is focued under ultrahigh vacuum (UHV) and in air. During UHV annealing to 850 °C, the NPs retain their morphology, chemical and optical properties, which makes them attractive in space mission and other applications. During air annealing to 800 °C, HfN NPs remain stable until 250 °C, which sets a limit for air-mediated use.

1. Introduction

Plasmonic nanomaterials offer the potential to significantly improve the efficiency of existing technologies, such as electronics and photonics, as well as to create new technological opportunities.[1–3] A plethora of optical, electronic, and quantum effects observed in plasmonic materials arise from the excitation of surface plasmons (SPs), coherent oscillations of electronic cloud at a metal–dielectric interface. The spatial confinement of the SPs in nanomaterials amplifies electric fields near the surface and increases light absorption at a certain frequency, leading to localized surface plasmon resonance (LSPR). Due to enhanced electric fields and light absorption, SPs generate optoelectronic phenomena with applications in sensing,[4,5] energy conversion,[6,7] catalysis,[8] and others.

Noble metals, such as silver and gold, remain the most ubiquitous and explored plasmonic materials owing to their strong light coupling in the visible part of the

P. Pleskunov, M. Protsak, Z. Krtouš, M. Tosca, K. Biliak, V. Červenková, D. Nikitin, J. Hanuš, J. Kousal, A. Choukourov
Department of Macromolecular Physics
Faculty of Mathematics and Physics
Charles University
V Holesovickach 2, Prague 18000, Czech Republic
E-mail: pleskunov@kmf.troja.mff.cuni.cz;
choukourov@kmf.troja.mff.cuni.cz

Z. Krtouš, L. Martinu
Department of Engineering Physics
Polytechnique Montreal
Montreal, Quebec H3T1J4, Canada

T. Košutová, M. Dopita
Department of Condensed Matter Physics
Faculty of Mathematics and Physics
Charles University
Ke Karlovu 5, Prague 12116, Czech Republic

M. Tosca
ELI Beamlines Facility
The Extreme Light Infrastructure ERIC
Za Radnicí 835, Dolní Břežany 25241, Czech Republic

M. Cieslar
Department of Physics of Materials
Faculty of Mathematics and Physics
Charles University
Ke Karlovu 5, Prague 12116, Czech Republic

spectrum (Vis) and a handful of well-adopted synthesis techniques. However, the high production overhead and a number of challenges posed by insufficient thermal and chemical stabilities have stimulated the exploration of transition metals and their compounds, including alloys, oxides, and nitrides.[9–11] In particular, some transition metal nitrides (TMNs) exhibit negative real-part permittivity in the visible and near-infrared (NIR) spectral regions, reflecting their metallic character.[12] TMNs have been envisioned as a promising alternative to noble-metal plasmonics because of their higher melting points, lower production-associated costs, and superior chemical robustness.

A pioneering work by Steinmüller–Nethl et al. became an onset for active exploration of plasmonic properties of TMNs.[13] Among many others, nitrides of the group four elements (TiN, ZrN, and HfN) have been generating vivid long-term interest as they show plasmonic metrics comparable to noble metals in the Vis/NIR regimes.[14] Furthermore, a pursuit for improved plasmonic response has led to a discovery of strong electron-phonon coupling, resulting in a temperature rise in a confined volume at the nanometer scale. For example, the localized heating phenomenon opened the possibility of using group four TMNs in further plasmonic applications, such as heat-assisted magnetic recording,[15,16] photothermal treatment,[17] and water desalination.[18]

Although group four TMNs have high melting points (typically about 3000 °C) and reportedly exhibit excellent chemical stability, their properties may not persist at the nanoscale. Nanomaterials can soften and/or liquefy at lower temperatures than their bulk counterparts because of the high surface-to-volume ratios.[9,11] This is obnoxious for many applications relying on nanoscale physical phenomena, including plasmonics and complementary metal-oxide semiconductor manufacturing. As such, it is imperative to establish the thermal stability of nanostructured TMNs.

The thermal stability of TMN thin films has been actively explored for a few decades.[19] For example, Krekeler et al.[20] demonstrated that epitaxially grown TiN films remain structurally stable at 1400 °C during annealing under vacuum conditions. A recent study on laser-induced photothermal reshaping of ZrN NPs reports on their thermal stability in the range of 1127–1827 °C, which is much higher than that of Au NPs (307 °C).[21]

The thermal stability of TiN, ZrN, and HfN NPs has not been systematically explored so far, and most of the existing studies have focused on annealing under a vacuum or in an inert atmosphere. For example, at least one report indicates that these NPs are stable upon annealing to 1000 °C in Ar during solid-state metathesis.[22] This trend is about to change nowadays, as the interest of scientific and industrial sectors gradually shifts toward the conditions under which the TMNs will be subjected to real-life applications, i.e., in air or dispersed in solvents. Recently, Diroll et al. used ultra-fast transient X-ray diffraction to evaluate the thermal stability of TiN NPs in air. The NPs remained structurally intact after annealing in air up to 300 °C, and up to 175 °C when suspended in water.[23] Despite efforts to improve their properties, there exists a significant knowledge gap on the thermal stability of nanostructured TMNs under various conditions. With this lack of understanding, the temperature limits of the plasmonic response of TMN NPs remain unclear, and the kinetics of thermally induced decay in the optoelectronic properties remains unknown.

Of the three TMNs of group four, HfN NPs are the least studied, partly because of the complexity of synthesis approaches.[24,25] Few studies have explored HfN NPs as plasmonic sensors,[26] plasmonic thermal hotspots,[27–29] direct absorption solar collectors[30] or catalysts for the electrocatalytic oxygen evolution reaction,[31] but they have not addressed the issue of thermal stability of the optoelectronic properties.

Our present study aims to offer a new approach to the synthesis of HfN NPs, which is based on reactive magnetron sputtering of Hf under elevated pressure of Ar/N$_2$ mixtures in the configuration of a gas aggregation cluster source, similar to our previous works.[32–34] A similar approach, involving cluster beam deposition techniques, was previously reported by Mainet et al.[35] for a size-selected synthesis of photoluminescent TiN NPs as well as by Reinholdt et al.[36] for plasmonic ZrN NPs. A brief summary of thermal stability of most common plasmonic TMNs prepared by reactive magnetron sputtering and cluster beam deposition methods is given in **Table 1** to reflect the current state of art and to underline the importance of the subject. Here, we go beyond the state-of-the-art and bridge the knowledge gap by probing the thermal stability of HfN NPs under annealing in UHV and air, while studying the effect on the structure, chemical composition, and optical properties. The computational predictions of the NPs optical response obtained by the finite-difference time-domain (FDTD) method are then compared with the experimentally measured data.

2. Results and Discussion

2.1. Optimization of the Deposition Parameters

The deposition process was optimized by performing experiments under different compositions of the working gas mixture (Ar/N$_2$) as described in Section S2 (Supporting Information). To study the influence of the gas phase content on the NP properties, three different working gas mixtures were selected for further analysis: 0 vol. % of N$_2$ as a reference point representing the metallic sputtering mode, 9.0 vol. % of N$_2$ which belongs to a transient mode between metallic and reactive modes, and 11.1 vol. % of N$_2$ that hallmarks the reactive mode.

2.2. Properties of the NPs

2.2.1. Morphology, Elemental Composition and Crystallinity of the NPs

Metallic Hf NPs grow predominantly into multi-faceted shapes, resembling hexagons at higher magnifications, while the transient and reactive modes of sputtering result in the diversity

I. Gordeev
Institute of Physics
Academy of Sciences of the Czech Republic
Cukrovarnická 10, Prague 16200, Czech Republic

M. Vorochta
Department of Surface and Plasma Science
Faculty of Mathematics and Physics
Charles University
V Holešovičkách 2, Prague 18000, Czech Republic

**ADVANCED
SCIENCE NEWS**

www.advancedsciencenews.com

**ADVANCED
OPTICAL
MATERIALS**

www.advopticalmat.de

Table 1. A comparison of characteristics of the HfN NPs with available literature on other refectory metal nitrides nanoparticles.

NP material	Synthesis technique/s	λ_{LSPR} position, nm	Thermal stability [T_{max}, °C]
TiN	laser ablation/evaporation cluster beam,[37] thermal plasma[38]	≈620[37]; ≈700[38]; ∼ 800[39]	250 (ambient air)[39]
ZrN	laser ablation/evaporation cluster beam,[36] PECVD[40]	≈570[36]	400 (ambient air)[40]
HfN (this work)	reactive dc magnetron sputtering	≈800	850 (vacuum); 250 (ambient air)
TaN	reactive dc magnetron sputtering	≈560[41]	unavailable

of NP shapes, involving multifaceted (close-to-spherical), cubic, and irregular structures (**Figure** 1a; Figure S2a–c, Supporting Information). The morphological changes are accompanied by changes in the size distribution, as seen from the SAXS data shown in Figure S2d–i (Supporting Information). The SAXS analysis provides a mean size (number-weighted size distribution) of 19 ± 4 nm (std. deviation) for sputtering in Ar, 23 ± 4 nm for the transient mode (9.0 vol. % of N_2), and 10 ± 3 nm for the reactive mode (11.1 vol. % of N_2; Figure 1b). These values are in good agreement with the statistical analysis of SEM micrographs of the same NPs (Figure S3, Supporting Information).

The elemental analysis of the NPs deposited under different conditions was performed using STEM-EDS. For the NPs sputtered in the metallic and transient modes, the results are shown in Figure S4 (Supporting Information), while STEM HDAAF images and the STEM-EDS maps of the NPs deposited in the reactive mode (11.1 vol. % of N_2) are shown in Figure 1c. Here, nitrogen appears to be homogeneously distributed within the NP volume. Surface oxidation is also observed in these NPs as a red(oxygen)-enriched halo.

Further analysis of the chemical composition was carried out by XPS. The spectra were acquired immediately after sample preparation without breaking the vacuum. These were compared with XPS spectra measured after one day of storage in ambient air. All XPS measurements were performed on the NP coatings with the overall thickness exceeding 200 nm to avoid potential effects imposed by the substrate. The detailed deconvolution and comparison of the high-resolution Hf 4f spectra for the NPs prepared in the metallic, transient, and reactive modes is given in Figure S5 in Section S3.2 (Supporting Information). Here, we focus on the HfN NPs prepared in the reactive mode (11.1 vol. % N_2). Only two pairs of peaks suffice to fit the spectrum. These belong to the dominant doublet of HfN and to the minor doublet of HfO_2 (Figure 1d). The $4f_{7/2}$ component of HfN is positioned at 15.5 eV (higher than 13.4 eV of metal Hf), indicating enrichment with the Hf—N bonds at the expense of the Hf—Hf bonding environment. Although it is impossible to completely avoid oxidation under our experimental conditions, the N/Hf ratio = 1.0 indicates that the NPs are stoichiometric. Contact with air leads to enhanced oxidation of these NPs, as illustrated in Figure 1e, re-
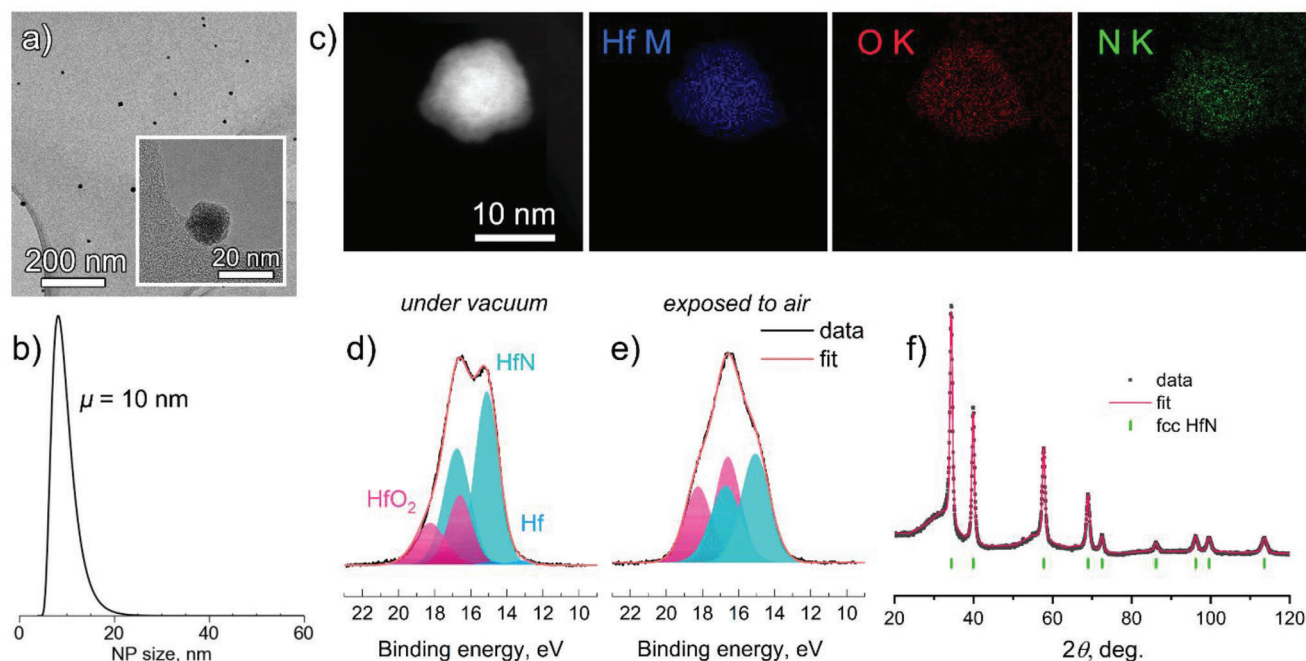

Figure 1. Characterization of the HfN NPs prepared at 11.1 vol. % of N_2 in the working gas mixture: HRTEM micrographs a), SAXS size distribution b), STEM HDAAF image and STEM-EDS elemental maps c); high-resolution XPS spectra of the core-level Hf 4f region acquired before d) and after e) the NP exposure to air; fitted X-ray diffraction pattern acquired on the HfN NPs with the corresponding ICDD reference f). The μ denotes the NP mean size.

**ADVANCED
SCIENCE NEWS**

www.advancedsciencenews.com

**ADVANCED
OPTICAL
MATERIALS**
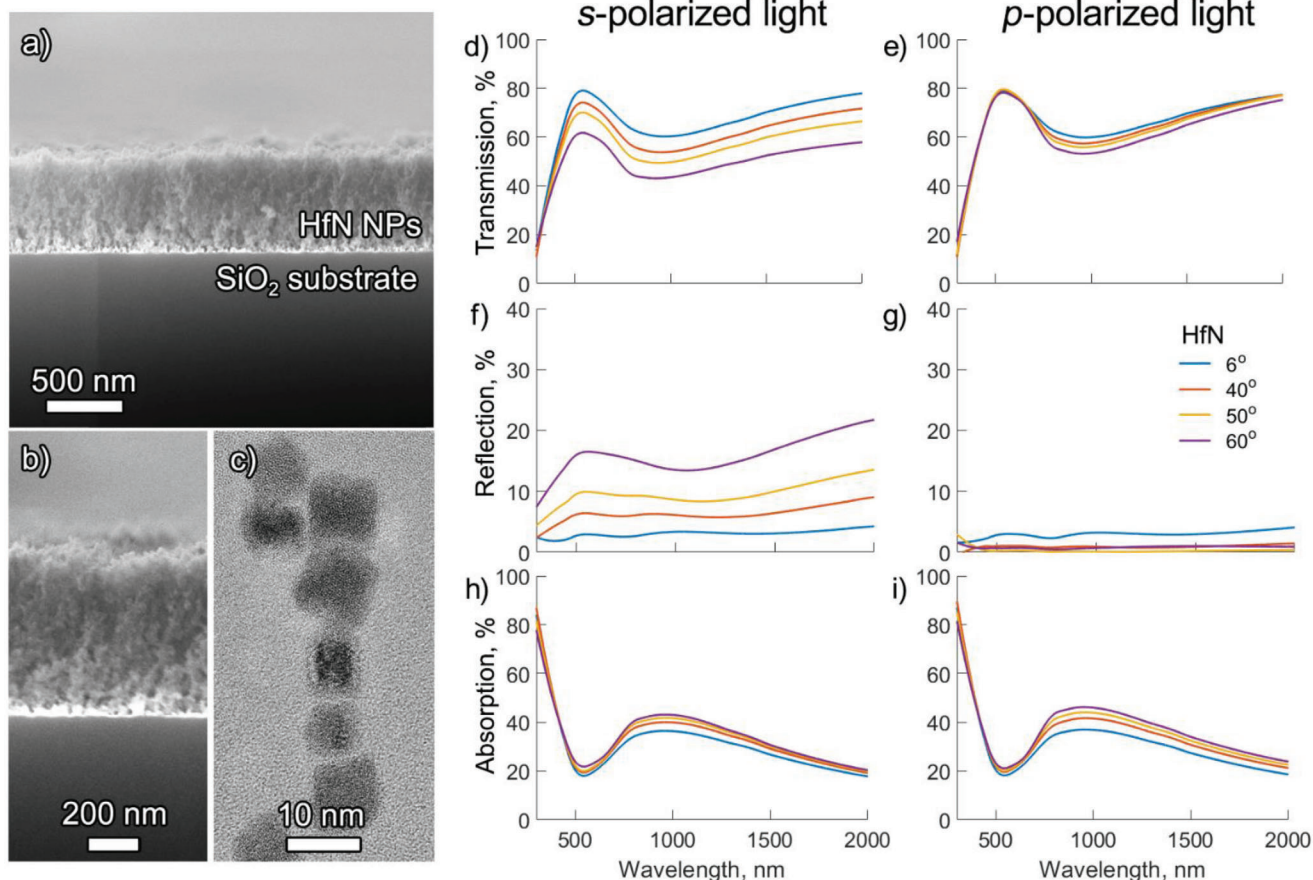
www.advopticalmat.de

Figure 2. SEM micrographs of different magnifications taken on HfN NP coatings in the cross-section orientation a,b); HRTEM micrograph of a chain comprised of HfN NPs c); multi-angle UV–Vis–NIR spectra recorded for *s* and *p* polarizations: d,e) transmission (*T*), f,g) reflection (*R*) and h,i) absorption (*A*) spectra of Hf and HfN NPs deposited onto SiO$_2$. Angles are given with respect to the substrate normal.

sulting in a decrease of the N/Hf ratio to 0.8. It should be noted that the quantitative XPS results must be interpreted with care, as they reflect the chemical states at the NP surface (a shell) rather than the NP core, owing to a substantial attenuation of the XPS signal with depth.

Besides the morphological changes, the addition of N$_2$ to the gas phase leads to microstructural changes in the NPs. Stoichiometric HfN NPs were prioritized over their nitrogen-deficient counterparts, and further analysis was performed on HfN NPs (and on metal Hf NPs when needed for comparison; see, for example, Figure S6, Supporting Information).

Sputtering in the reactive mode results in the formation of HfN NPs that consist predominantly of the *fcc* HfN phase (space group 225, PDF-4 00-025-1410) with an exiguous contribution from HfO$_2$ manifested via a broad peak at ≈30° in the XRD patterns (Figure 1f). However, the overall contribution of HfO$_2$ is very small and its crystallinity is limited, which makes it impossible to reliably quantify this phase using XRD. Thus, we exclude this phase from the analysis. The measured lattice parameter 4.514(1) Å was found to be similar to that of cubic stoichiometric HfN in the bulk form ($a = 4.518$ Å).[42] The formation of a stable *fcc* phase with lattice constants close to the equilibrium values indicates that the thermalization of HfN NPs is slower compared to

that of Hf NPs, probably due to an additional energy gain given by the high enthalpy of the Hf-N bonds formed.

2.2.2. Optoelectronic Properties of the NPs

The HfN NP coatings were deposited onto SiO$_2$ substrates to study their optical properties. First, the structure of the HfN coating was characterized using SEM to set a groundwork for the spectrophotometric measurements. The cross-section SEM micrographs of different magnifications are shown in **Figure 2a,b**. The thickness of the coating was found to be ≈640 nm. SEM analysis also revealed a porous coating structure arising from a soft-landing deposition regime.[43] In such a regime, the kinetic energy per atom is substantially lower than the cohesive energy. Thus, no deformation of the NPs occurs as they arrive at the substrate, as documented by HRTEM imaging of a chain consisting of multiple HfN NPs (Figure 2c).

According to the ellipsometry measurements carried out on similar samples but deposited on Si wafers, the coating porosity seems to be a function of its depth. Porosity at the bottom of the coating (≈30 nm) is estimated to be between 0.1 and 0.2 (the void fraction), while it reaches 0.7 in the layers deposited above. The

**ADVANCED
SCIENCE NEWS**

www.advancedsciencenews.com

**ADVANCED
OPTICAL
MATERIALS**

www.advopticalmat.de

latter value is in line with previous theoretical predictions and measurements conducted on NP-based films.[44,45]

Preliminary optical measurements conducted on the Hf and HfN NP coatings revealed that diffusive scattering remained below a sensitivity limit of the instrument. We note that the interaction of light with NPs smaller than the wavelength can lead to scattering events,[46,47] which are difficult to observe. One particular reason is the dominance of the absorption efficiency over the scattering efficiency for small-sized particles as it can be inferred using the quasi-static approximation.[47] Also, the Mie theory highlights a quick fall-off of the scattering cross-section due to the dissipative losses if the NP size is small. Recent studies have shown that HfN can facilitate light-to-heat conversion through thermoplasmonic relaxation.[18,48] The latter stems from a less negative real part and a higher imaginary part of the HfN complex permittivity relative to noble metals, resulting in a lossy plasmonic response.[29] Our FDTD calculations (discussed in detail later) conducted on a single 10 nm sized HfN NP point to a two-order difference between the absorption and scattering efficiencies. We hypothesize that due to a combination of small NP size and lossy plasmonic nature of the HfN, diffusive scattering was not registered. Thus, the scattering contribution was ignored and only the results obtained on the UMA-enabled instrument were used for the analysis.

The multi-angle UV–Vis–NIR spectra recorded on the NP coatings are presented in Figure 2d-i. The polarization effects can hardly be expected in individual NPs, although larger agglomerates (groups or chains of NPs) might give rise to differences between s- and p- polarizations. Thus, the optical spectra in both s- and p- polarizations were recorded. The transmission (T) and reflection (R) spectra show the angular dependence, with the reflection increasing at higher angles for the s-polarization and decreasing for the p-polarization. This trend aligns with a Fresnel T/R coefficients dependency on the angle of incidence; however, the samples coated with the NPs exhibit lower reflectivity as compared to a bare SiO_2 substrate (Figure S7c,d, Supporting Information). Unlike continuous metallic films, the coatings of the HfN NPs are porous, and the combination of small thickness and high porosity suppresses the coating reflectivity (Figure 2f,g).

In contrast to metallic Hf NPs (Figure S8a,f, Supporting Information), the UV–Vis–NIR spectra of the HfN NPs show a strong transmittance minimum in the near-IR range, which is inversely replicated by the absorption maximum (Figure 2d,i). The minimum reflectivity aligns with the transmission minimum (absorption maximum) centered at $\lambda \approx 970$ nm. At $\lambda < 500$ nm, transmission subsides, and absorption dominates the spectra.

HfN is known to exhibit optoelectronic features of metals: its conduction and valence bands are partially overlapped, and the Fermi level is located in the conduction band, pointing to the availability of free carriers.[14] Therefore, the near-IR absorption band can be attributed to intraband electron transitions and LSPR, whereas the absorption at $\lambda < 500$ nm can be associated with interband transitions. Here, the absorbed photons have enough energy to transit from N $2p$-states dominating the valence band to unoccupied Hf $5d$-states close to the Fermi level.[49]

Our UPS measurements on the HfN NPs (Figure S9, Supporting Information) revealed an energy difference of 2.9 ± 0.1 eV between the Fermi level and the maximum of the valence band (E_F-E_{VBM}), which correlates well with the theoretical values of

3.1 eV for the interband transitions,[14] but larger than the optical crossover at $\lambda < 500$ nm (> 2.5 eV). The deviation might be explained by the fact that the UPS analysis depth is limited to 2–3 nm by a short inelastic mean free path, and the spectra reflect mostly the states found in the oxidized NP shell.

Interestingly, the UV–Vis–NIR spectra of HfN NPs resemble those of commercially available optical green filters with potential use in cameras or displays.[50] Regardless of the incident light polarization, the optical properties of the HfN NPs remain consistent, which is seen as an advantageous feature in optical filter applications.

HfN is often recognized as a plasmonic alternative to Au owing to its larger absorption (σ_{abs}) and scattering (σ_{scatt}) cross-sections as also evidenced by our FDTD calculations performed for a single 10 nm sized HfN and Au NPs (Figure S10, Supporting Information). This result is consistent with previous reports on the photophysical dynamics of HfN and is attributed to a higher imaginary permittivity of HfN relative to noble metals,[29] because the absorbed power is proportional to the product of the square of the imaginary permittivity and the electric field. However, the formation of the 2 nm thick HfO_2 shell reduces the HfN absorption efficiency down to that of Au NP and red-shifts the LSPR peak slightly. The contribution of the σ_{scatt} to the light extinction can be safely neglected, as there exists nearly two orders of magnitude difference between the σ_{abs} and σ_{scat}.

To further explore the oxidation effects on the optical response of HfN NPs, a model of 10 nm sized core–shell HfN@HfO_2 NP was used, where the oxide shell thickness gradually grows at the expense of the NP core. The increase of the shell thickness red-shifts the σ_{abs} and σ_{scatt} and trims their magnitudes (Figure S11a,b, Supporting Information), which is reflected by the red-shift, broadening, and magnitude loss of the extinction band (**Figure 3a,b**). As HfO_2 becomes the dominant phase, the contributions of σ_{abs} and σ_{scatt} become comparable, leading to a development of an extinction peak in the UV region (< 400 nm) as shown in Figure 3c. This extinction can be attributed to the Rayleigh scattering on the HfO_2, similar to the previously reported scattering on the TiO_2 nanocrystals in the UV range.[51]

Despite the simplicity of the model in use, it allows for obtaining of the optical response close to that observed experimentally for the oxidized HfN NPs also matching the previous theoretical reports.[28,29] The best match is obtained for the oxide shell thickness of ≈4.5 nm (Figure 3b), which overestimates the reality, as the model does not account for gradual oxidation and optical properties of HfN_xO_y formed on the surface of the NPs. The red-shift of LSPR is attributed to a higher refractive index (RI) of HfO_2 (≈2.0) as compared to ambient air (≈1.0).

In contrast to the oxidation, a change in the NP size primarily affects the magnitude of the extinction band, while having a negligible imprint on its position, except for a small blue-shift of the band as the NP size is decreased (Figure S12, Supporting Information).

The electromagnetic coupling between densely packed NPs is known to red-shift the LSPR of plasmonic NPs by hundreds of nanometers.[52] Such a near-field interaction between NPs is highly distance-dependent and the interparticle distance stochastically variates for multilayers of NPs used for our spectrophotometric measurements. The plasmon hybridization model used to describe coupling also highlights the asymmetry introduced
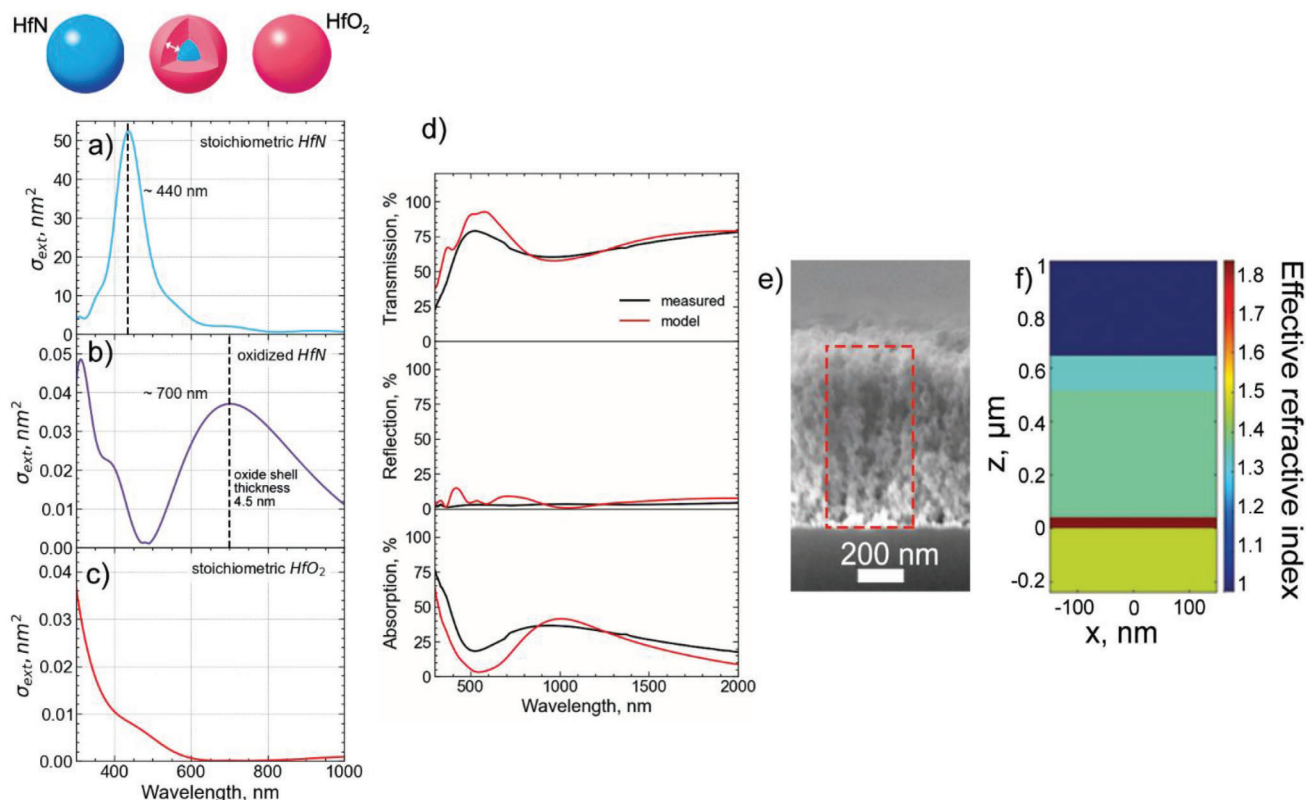
**ADVANCED
SCIENCE NEWS**

www.advancedsciencenews.com

**ADVANCED
OPTICAL
MATERIALS**

www.advopticalmat.de

Figure 3. FDTD-calculated extinction cross-sections for: a stoichiometric HfN NP a), oxidized HfN b), stoichiometric HfO$_2$ c); a comparison between experimentally measured and model transmission, reflection, and absorption spectra of the HfN NP coating d); SEM micrograph taken on the HfN NP coating deposited onto SiO$_2$ substrate in the cross-section orientation e) and effective refractive index map obtained by the ellipsometry f).

by dimer formation. The orientation of the electric field relating to the interparticle axis could cause bonding/nonbonding interactions, producing red/blue shifts.[53] We probe into electromagnetic coupling using a dimer comprised of equally-sized HfN NPs embedded in air and HfO$_2$ to account for effects induced by the medium RI. Regardless of the RI, electromagnetic coupling begins at the interparticle distances below 10 nm, manifesting via the red-shift and indicating a bonding-like coupling observed when the electric fields are oriented along the interparticle axis for a given NP pair.[53–55] For HfO$_2$, the red shift is more pronounced due to a higher RI (Figure S13, Supporting Information). The HRTEM measurements reveal the maximum oxide shell thickness of 3 nm, resulting in a 6 nm interparticle distance, which lies within the coupling limit and, therefore, near-field interactions in the multilayers can further shift the LSPR toward the long-wavelength end of the visible spectrum part.

Taken all the cases together, the plasmonic response of HfN NPs is governed primarily by the NP oxidation and by electromagnetic coupling responsible for additional peak broadening. The interparticle distance and the NP size dispersity do not provide significant flexibility for tuning the optical response of the HfN NPs and should be minimized if sharper peaks are desired. We also hypothesize that it is possible to engineer optical properties by suppressing the NP oxidation via embedding the NPs into an oxygen-free protective matrix or by coating them during the synthesis. For example, silicon nitride (Si$_3$N$_4$) or aluminium

nitride (AlN) can be used depending whether transparency in the visible or near-infrared spectral regions is desired.[56,57]

Finally, an in-depth analysis of the HfN NPs was carried out using spectroscopic ellipsometry to extract the optical parameters of the material, specifically the refractive index (n) and the extinction coefficient (k), and to consolidate our previous findings by investigating the influence of the coating porosity on its optical response. The details of constructing the ellipsometry model are given in (Section S1.2.5, Supporting Information). The obtained optical parameters were then incorporated into the FDTD model of the NP coating to calculate its transmission, reflection, and absorption spectra. The calculated spectra match closely the measured spectra with minor magnitude deviations (Figure 3d). The reflection oscillations in the visible and NIR ranges are caused by interferences related to the finite discretization used in the model, while in reality, there is no distinct interface between individual layers in the NP coating.

In addition, our calculations show that the porosity reduces the effective refractive index (n_{eff}) of the coating (Figure 3e,f). On one hand, the bottom layer is estimated to have $n_{eff} \approx 1.8$, which is below the theoretically predicted value for the HfN ($n = 2.4$). On the other hand, the effective refractive index of the two layers above is ≈ 1.4, with a minor variation between the topmost and the middle layers. This reflects the real coating structure where gaps between the NPs are smaller for the bottom layer and larger for the top layers.
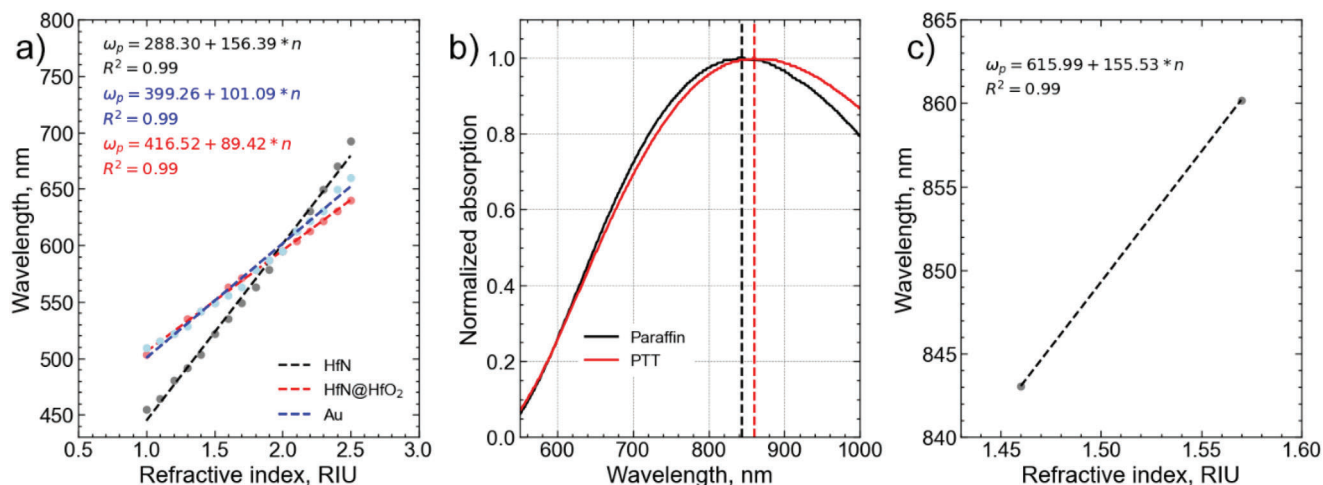
**ADVANCED
SCIENCE NEWS**

www.advancedsciencenews.com

**ADVANCED
OPTICAL
MATERIALS**

www.advopticalmat.de

Figure 4. Linear regression analysis of the extinction peak maxima for HfN and Au a); normalized absorption of HfN NPs deposited into the liquid paraffin and PTT b); linear regression fit of the (c). The plasmon wavelength shift is denoted as ω_p.

Plasmonics effects are widely used in LSPR transducers for chemical and biological sensing applications. In this section, we investigate the potential of HfN NPs for plasmonic sensing. The LSPR transducers operate by exploiting a dependence of the optical response (i.e., LSPR band position, intensity, and shape) on the dielectric properties of a surrounding. In particular, they are intended to be sensitive to the changes induced by the binding of analyte molecules or a medium (air, solvent) displacement. In addition, the performance of the sensor also depends on the distance from its surface due to decay of the evanescent plasmon field, which extends from the metal structure into the surrounding medium. In general, the decay is influenced by the physical parameters and the material of the NPs and can be approximately described by:[58,59]

$$\lambda_{LSPR} = m \cdot \Delta n \cdot \left(1 - e^{-\frac{2d}{d_{decay}}} \right) \tag{1}$$

where λ_{LSPR} is the plasmon resonance maximum wavelength shift, m is the refractive index sensitivity of the sensor, Δn represents a difference between the refractive index of the adsorbate and that of the surrounding medium, d is the adsorbate layer thickness, and d_{decay} is the plasmon effective decay length.[60,61]

If the decay length is smaller than the adsorbate layer (AL) thickness, then the sensor response to binding event will be rather weak due to a rapid exponential decay of the field. On the contrary, if the decay length is large compared to the AL thickness, the analyte molecules will occupy a limited fraction of the sensing volume, leading, again, to a subtle response. Typically, to achieve the optimal transducer performance, the refractive index sensitivity needs to be maximized and the decay length should match the recognition interface (for example, an antibody bound to the NP) dimensions.

When an NP is embedded in a matrix, one can treat the effective thickness d as infinite and, thus, the sensor response simplifies to: $\lambda_{LSPR} = m \cdot \Delta n$. This provides a concept of a bulk sensitivity of the sensor. First, we use FDTD to calculate the bulk sensitivities of the stoichiometric HfN, oxidized HfN (2 nm HfO$_2$ shell thickness) and Au NPs embedded into matrices with

variable refractive indices. Our calculations show the LSPR peak red-shifts as the refractive index of the medium increases from 1.0 to 2.5 refractive index units (RIU) for the stoichiometric and oxidized HfN as shown in Figure S14 (Supporting Information). In both cases, the response is linear across the entire refractive index range. The bulk RI sensitivity of the stoichiometric HfN is 156.39 nm RIU^{-1} (**Figure 4a**), which is higher than 101.09 nm RIU^{-1} calculated for the Au NP at the same conditions and 92.58 nm RIU^{-1} reported for the Au-based sensor.[62] However, surface oxidation significantly hinders the RI sensitivity of the HfN NPs. For the HfN NP wrapped by a 2 nm thick HfO$_2$ shell, the bulk RI sensitivity drops to 89.42 nm RIU^{-1}, which is noticeably lower than the calculated and measured sensitivity of the Au NPs.

To experimentally explore the bulk sensitivity of the HfN NPs, we deposited them directly into vacuum-compatible host liquids with different refractive indices: low-viscosity paraffin (refractive index 1.46) and pentaphenyl trimethyl trisiloxane (PTT, refractive index 1.57). In this case, we expect HfN NPs to be less oxidized than those stored in air because the host liquid serves as a barrier, limiting the diffusion of molecular oxygen and water toward NPs. The optical absorption of the prepared nanofluids was measured using UV–Vis as shown in Figure 4b. Although the data set is limited to two data points, the experimentally measured RI sensitivity is estimated to be 155.53 nm RIU^{-1} (Figure 4c), which closely matches our theoretical predictions for the stoichiometric HfN (Figure 4a).

In practice, the detection usually occurs within the first 10 nm away from the surface. To estimate the plasmon decay length of the HfN NPs, we fit the calculated plasmon shift (Figure 4c) using equation 1, which gives m of 237.67 nm RIU^{-1} and d_{decay} of 4 nm, setting thickness limits for applications in chemical or biological sensing.

2.3. Thermal Stability of the HfN NPs

The presence of oxygen and disorder in the topmost layers of HfN NPs may strongly affect their thermal stability, especially under
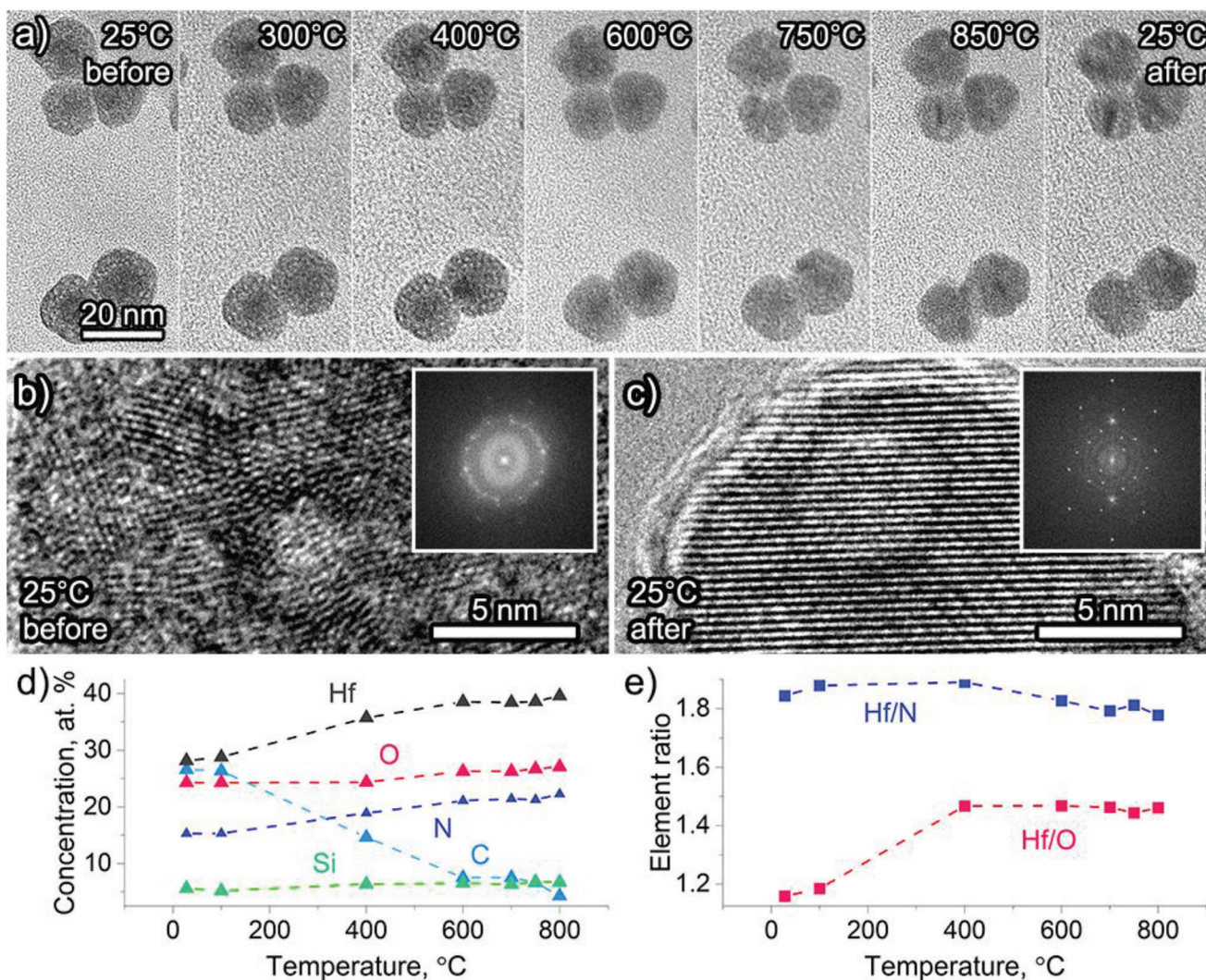
Figure 5. HRTEM of HfN NPs: a) during annealing under UHV; b,c) magnified HRTEM micrographs taken on a single NP before and after annealing; elemental content of the HfN NPs as determined by XPS during annealing in UHV: elemental atomic concentrations d) and Hf/N and Hf/O ratios e). The dashed lines are guides for the eyes. Insets show FFT patterns obtained from HRTEM micrographs taken on the single NP before and after annealing.

an ambient atmosphere. We used post-deposition processing to observe the thermally induced phenomena in the HfN NPs. Annealing under UHV is a powerful, yet widely adopted technique for tuning the crystallinity of TMN thin films and for defect-rich microstructure refinement procedures, such as thermal facet healing,[63] and defect pattern engineering.[64] On the other hand, high-temperature annealing in air may deteriorate the chemical composition of the NPs, but this issue has not been explored in depth yet.

2.3.1. Thermal Stability Under UHV Conditions

Figure 5a shows the TEM micrographs of a group of HfN NPs acquired at different temperatures under UHV, starting from RT. Tracing the structural evolution with temperature, one can notice that the UHV annealing neither impacts the NP shape nor causes migration or coalescence of individual NPs, highlighting the re-

fractory nature of HfN. However, the microstructure appears to be influenced by the temperature, as the darker core of the initial NPs becomes almost indistinguishable at about 750 °C. A closer look at higher magnification provides more details on the underpinning phenomena. The HRTEM micrographs of a single NP at RT prior to and after annealing are shown in Figure 5b,c. Initially, the HfN NPs are polycrystalline and consist of randomly oriented crystalline domains. During UHV annealing, the NPs undergo grain coalescence and atomic rearrangements, causing visible grain boundaries to vanish. Atomic diffusion caused by the thermal energy influx significantly enhances the crystallinity of NPs and their microstructure becomes more ordered and uniform. The ordered microstructure persists after cooling, as seen in the FFT patterns in Figure 5b,c, pointing to an energetically favorable atomic arrangement established. Together with the lack of morphological changes in NPs, a highly ordered crystalline structure is seen as a highly favorable outcome of such treatment, as it should not substantially affect the optical properties of HfN
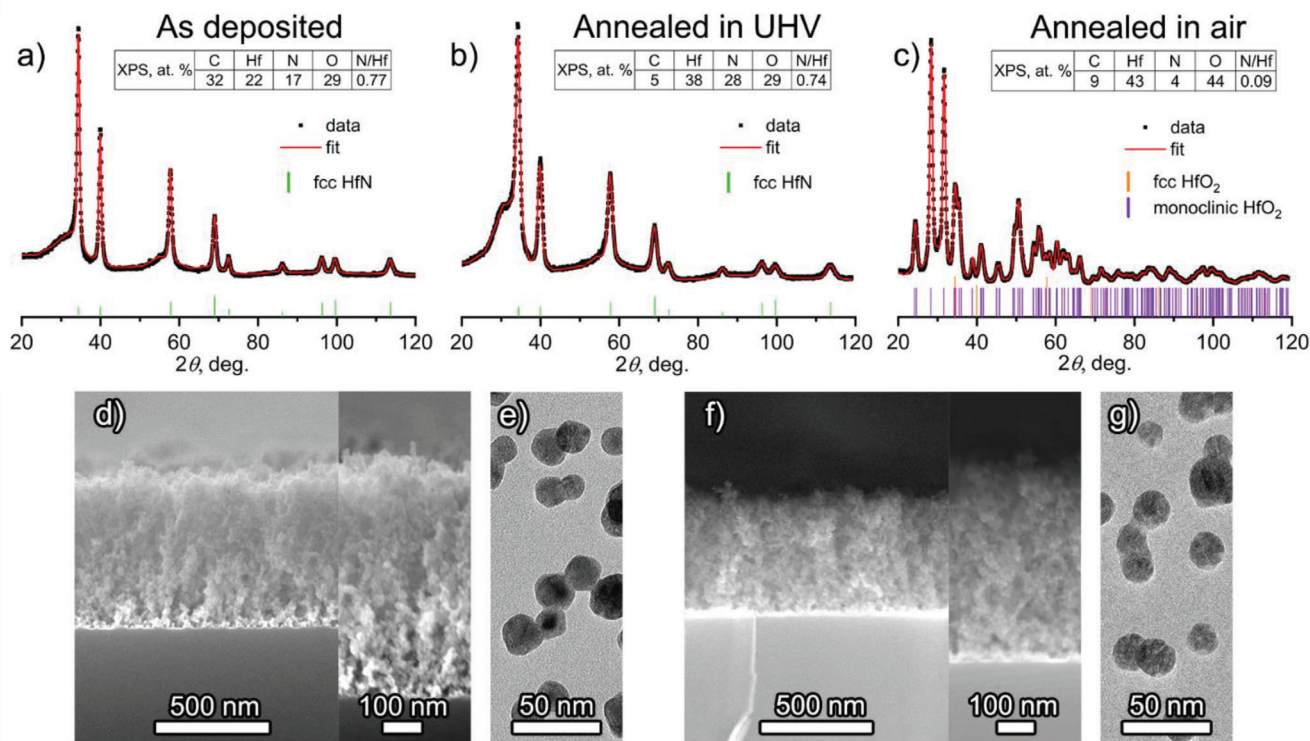
Figure 6. X-ray powder diffraction patterns acquired on HfN NPs before a) and after annealing under UHV at 850 °C b); and after annealing in air at 800 °C c); cross-section SEM and HRTEM micrographs of the HfN NPs before d,e) and after the annealing in air at f,g) 800 °C. Insets show the XPS elemental composition.

NPs. This assumption is validated by our UV–Vis–NIR measurements, discussed later.

Being a local technique, HRTEM provides an atomic-scale structural resolution. We augment the electron microscopy measurements with a complementary XPS analysis. Herein, the multilayers of HfN NPs deposited on the Si substrate were heated under UHV conditions, matching those observed by HRTEM. The high-resolution XPS spectra of the core-level Hf 4f, N 1s, and O 1s regions acquired during UHV annealing are shown in Figure S15 (Supporting Information), while the changes in the elemental content are shown in Figure 5d,e. The initial carbon contamination is almost eliminated above 600 °C, exposing the original surface, which is expectedly oxidized. The elemental analysis does not show changes in the oxygen content within the experimental error, evidencing that the oxidative processes, even if present, are limited under UHV. Changes in the Hf/N ratio are also too small to draw specific conclusions about changes in the surface nitriding. Given these points, these HfN NPs show strong potential for high-temperature applications under UHV conditions, including particle accelerators or space mission applications.

2.3.2. Thermal Stability in Air

To evaluate the thermal stability of HfN NPs in air, we performed XRD and XPS analysis on the as-deposited HfN NPs (**Figure 6a**), after their annealing under UHV at 850 °C (Figure 6b)

and in the air at 800 °C (Figure 6c). Nearly identical diffraction patterns were obtained for the as-deposited and UHV-annealed samples, indicating good retention of the *fcc* HfN phase (space group 225, PDF-4 00-025-1410). A closer look at the diffraction patterns reveals a slight enhancement of the oxidation marker represented by a tail at $\theta \approx 30°$, which agrees with the minor oxidation revealed by the Hf 4f XPS spectra. The XPS Hf/N ratio remains almost unchanged, which also confirms the chemical stability under UHV annealing. On the contrary, annealing in air results in a drastic change in the diffraction pattern (Figure 6c). The NP crystal structure is converted to monoclinic HfO$_2$ (space group 14, PDF-4 04-004-3850), with a slight contribution from residual unconverted *fcc* HfN and minor inclusions of *fcc* HfO$_2$ (space group 225, PDF-4 00-053-0560). The chemical changes are further supported by the XPS data, which show a drastic decrease in the nitrogen content.

To investigate thermally-driven morphogenesis of the HfN NPs, we performed HRTEM and cross-section SEM imaging of the NPs before and after the annealing in air. The SEM analysis was performed on the coatings, whereas the TEM analysis was performed on individual NPs transferred from the coating to the grids by scratching. The annealing in air results in the densification of the coating as shown in Figure 6d,f. The thickness is decreased from ≈640 nm for as deposited coating to ≈510 nm for the annealed coating. We attribute this effect to a partial coalescence of the individual NPs as documented by the TEM measurements (Figure 6e,g). Nevertheless, NPs mostly retain their
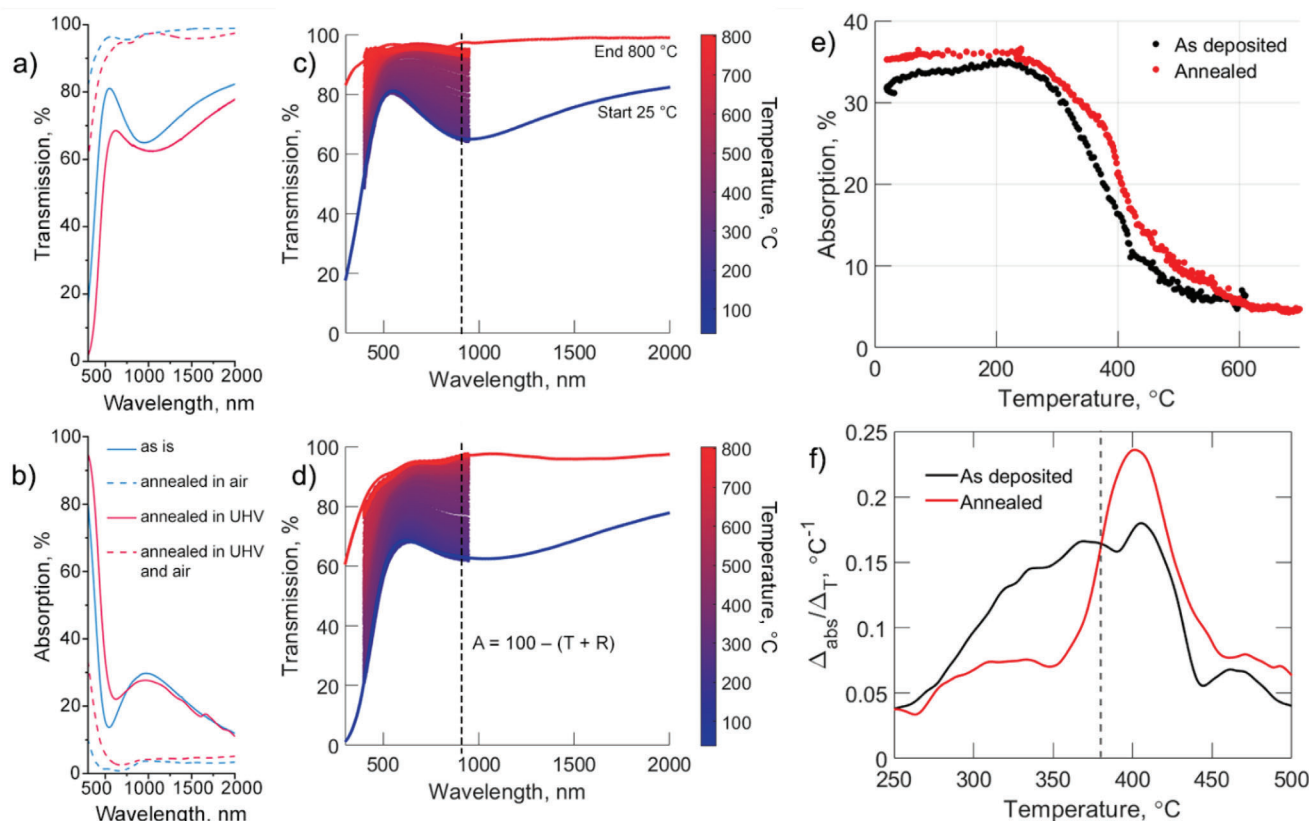
ADVANCED
SCIENCE NEWS

www.advancedsciencenews.com

ADVANCED
OPTICAL
MATERIALS

www.advopticalmat.de

Figure 7. UV–Vis–NIR transmission a) and absorption b) spectra of HfN NPs on SiO$_2$: as-deposited (as is), annealed in air, annealed in UHV, and annealed sequentially in UHV and air; UV–Vis–NIR transmission spectra of as-deposited c) and annealed in UHV d) HfN NPs on SiO$_2$ during heating in air; the spectra acquired during the annealing are colored and overlapped with the spectra recorded at the steady-state conditions a,b); the dependence of absorption on the sample temperature at $\lambda = 910$ nm for the as-deposited and UHV-annealed samples e); the first-order derivatives of the absorption curves shown under e) with respect to the temperature.

morphology during the annealing. A similar effect was previously observed for the magnetron-sputtered Nb NPs by in situ X-ray scattering.[65]

The structural and chemical changes are manifested in the optical properties. UV–Vis–NIR measurements were performed on four types of samples deposited onto quartz substrates. First, as-deposited HfN NPs were measured. Then, the same HfN NPs were measured after annealing in air. The third measurements were performed on the as-deposited HfN NPs after their annealing under UHV. These UHV-annealed NPs were subsequently subjected to air annealing, and the final measurement was performed. The corresponding transmission and absorption spectra are shown in **Figure 7a,b**. Importantly, results confirm that the optical properties of HfN are retained after UHV annealing, because the spectrum of the as-deposited sample is similar to that of the sample annealed under UHV, with the LSPR band retaining its position. After annealing in air, the plasmonic properties of HfN NPs are degraded for both as-deposited and UHV-annealed samples. In this case, transmission becomes strongly enhanced throughout the optical range and only traces of the plasmonic band can be distinguished.

To explore the degradation kinetics, optical transmission spectra were recorded during the heating of the as-deposited

(Figure 7c) and UHV-annealed samples (Figure 7d) in air. Numerous spectra were obtained and colored from blue (RT) to red (800 °C) to produce color gradient maps. It should be noted that, in this case, the instrument allowed the measurements limited to $\lambda = 950$ nm only. After the baseline correction, the newly obtained spectra were matched to the UV–Vis–NIR spectra of Figure 7a (shown by solid blue and red lines) for better visualization of the thermally-induced changes. The wavelength of $\lambda = 910$ nm close to the absorption maximum was selected and the evolution of the transmission at the selected wavelength was traced with the sample temperature. Then, the transmission was converted to the absorption as $A = 100 - (T + R)$ and plotted as a function of the temperature as shown in Figure 7e.

Both samples retain the original absorption level until 250 °C, which marks the stability point for the HfN NPs. Subsequently, the absorption degrades for both samples, and at 500 °C it reaches very low values. Interestingly, the degradation rate is different for the two samples, as can be inferred from the slope of the absorption decays. To quantify the difference, we differentiated the data between 250 °C and 500 °C, and the derivatives are shown in the inset of Figure 7e. The absorption of the UHV-annealed HfN NPs decays slower in the range of 250–350 °C, pointing to a higher resilience of these NPs to oxidation. However, at higher tempera-

**ADVANCED
SCIENCE NEWS**

www.advancedsciencenews.com

**ADVANCED
OPTICAL
MATERIALS**

www.advopticalmat.de

tures, the degradation rate spikes beyond that of the as-deposited NPs, and then the decay rates of both samples closely follow each other with a small discrepancy.

These findings confirm the stability of HfN NPs in air up to 250 °C, highlighting the positive effects brought about by UHV annealing. We associate better stability and slower degradation rates with thermally driven structural refinements, resulting in the formation of well-ordered, highly crystalline HfN with fewer defects. Therefore, our findings are in line with the conventional notion of high-temperature stability of TMN, but we set even more strict conditions: HfN NPs can be useful in high-temperature air-mediated applications, provided that the temperature does not exceed 250 °C. We also believe that increasing the NP size could be one of the possibilities to further increase their thermal stability in the air. Interestingly, the conversion of HfN to HfO_2 at higher temperatures offers a route toward mesoporous oxide coatings, which is another exciting class of materials with numerous applications.

3. Conclusion

Reactive dc magnetron sputtering of the Hf target in Ar/N_2 mixtures was combined with a gas aggregation technique to produce HfN NPs in lieu of conventional thin films. The morphology, microstructure, and composition of the NPs were tailored by adjusting the N_2 content in the working gas. Three sputtering modes were identified while optimizing the deposition conditions. Sputtering in pure Ar (the metallic mode) renders 19 nm sized, multifaceted, crystalline Hf NPs which oxidize upon contact with air with the formation of the HfO_2 shell. In the transient mode (9.0 vol. % of N_2), the NPs showcase a diverse morphology ranging from close-to-cubic to irregular and ramified shapes. Finally, the reactive sputtering mode (11.1 vol. % of N_2) produces the stoichiometric HfN NPs with a mean size of 10 nm, characterized by multifaceted and cubic shapes and the crystalline structure of *fcc* HfN.

The plasmonic properties of these NPs were evident through a broad optical absorption band in the red/NIR range, attributed to intraband transitions and LSPR. The energy difference of 2.9 eV between the Fermi level and the valence band maximum correlates with the onset of optical absorption at wavelengths below 500 nm. The transmission and reflection of the NP coatings remained consistent regardless of the angle of incidence or polarization of the light.

In addition, we use the FDTD method to predict the HfN NPs optical properties and the imprint of post-deposition oxidation on them. The results also indicate that plasmonic properties can be engineered by controlling the NP chemical composition and/or preventing oxidation. The LSPR shift and broadening can be bypassed with increasing the interparticle distance, for example by embedding the HfN NPs into an oxygen-free matrix. Finally, the calculations and experiments suggest that the HfN NPs can potentially be used for chemical and biological sensing as they exhibit a relatively high refractive index sensitivity, yet the oxidation and limited plasmon decay length should be considered.

Beyond synthesis and optical properties, the study delved into the thermal stability of HfN NPs employing a combination of HRTEM, XPS, and UV–Vis–NIR. During annealing under ultrahigh vacuum conditions, the HfN NPs demonstrated high mor-

phological and chemical stability up to 850 °C. At 600 °C, a structural transformation occurred, leading to a highly ordered state due to atomic reconfiguration, although optical properties remained largely unchanged. The thermal stability study extended to annealing in air, revealing that HfN NPs preserved their optical properties up to 250 °C, beyond which chemical and structural transformations ensued. A comparison between as-deposited samples and those annealed preliminarily under UHV demonstrated better resistance of the latter to thermal degradation, attributed to a refined crystalline structure. However, both types of NPs became deficient in nitrogen and oxidized to HfO_2 at temperatures exceeding 500 °C. Despite the NPs losing plasmonic characteristics, this transformation opened a new route to highly porous transition metal oxide coatings.

4. Experimental Section

Synthesis of NPs: Metallic Hf and HfN NPs were synthesized using a custom-built magnetron-based gas aggregation cluster source (GAS, schematically shown in Figure S1a, Supporting Information) mounted onto a deposition chamber.[32,66–70] The metallic Hf NPs were synthesized in an argon (Ar) atmosphere, while the HfN NPs were prepared by adding nitrogen to Ar. The magnetron operated in constant current mode at 500 mA throughout all experiments. The main deposition conditions were characterized by the quartz crystal microbalance (QCM) readings and the target bias values. (Figure S1b, Supporting Information). More details about the experimental setup are available in the (Section S1.1, Supporting Information) as well as in the preceding publications from group.[32,65]

To prepare the samples, a substrate was introduced into the deposition chamber via a load-lock while facing normally the flow of NPs. The NPs were collected on multiple types of substrates, including c-Si (10 × 10 mm, phosphor doped, <100> oriented, Si wafer pieces with native oxide, OnSemi), quartz substrates (UV-grade, fused silica, 10 × 10 mm, 0.5 mm thick, SPI Supplies) and Transmission Electron Microscopy (TEM) grids (Lacey Carbon Coated Cu Mesh for general TEM imaging and Ni Mesh for in situ TEM measurements during annealing the samples in vacuum, SPI Supplies).

For refractive index sensitivity measurements, HfN NPs were directly embedded into a host liquid to create nanofluids (NFs), employing a method detailed in previous works.[68,69] Two vacuum-compatible host liquids with different refractive indices were utilized: low-viscosity paraffin (CAS-No: 8042-47-5, refractive index 1.46, Sigma–Aldrich) and pentaphenyl trimethyl trisiloxane (PTT, CAS-No: 3390-61-2, refractive index 1.57, Kurt J. Lesker).

Characterization of NPs: The morphology and structure of the NPs were studied by High-Resolution Transmission Electron Microscope (HRTEM, 2200FS, Jeol Ltd.) with an FEG cathode operated at 200 kV of acceleration voltage. The samples were analyzed as-deposited and during annealing under an ultrahigh vacuum with a maximum temperature of 850 °C. A detailed description of HT-HRTEM measurements can be found in the (Section S1.2.1, Supporting Information). In addition, the NP morphology was analyzed using a Scanning Electron Microscope (SEM, JSM-7200F, Jeol Ltd.). SEM measurements were conducted in a secondary electron imaging mode (SE mode), capturing both top-view and cross-section sample orientations at a 25 kV acceleration voltage (V_{acc}) for metallic Hf and HfN NPs. The annealed NPs were measured at a reduced V_{acc} of 10 kV to mitigate charging effects arising from the dielectric nature of HfO_2.

The Scanning Transmission Electron Microscopy (STEM-EDS, Centurio Large Angle SDD-EDX detector) and X-ray Photoelectron Spectroscopy (XPS, Specs GmbH.) were used to analyze the elemental composition of the as-deposited NPs. Similar to the TEM measurements, the XPS analysis employed two approaches. In the first approach, the NPs were analyzed immediately after preparation without breaking vacuum and after 24 h of storage under atmospheric conditions. The second approach in-

volved conducting XPS analysis on several day-aged HfN NPs during their UHV annealing to 850 °C to align with the conditions of the HT-TEM measurements. In both cases, wide and high-resolution (HR) spectra were acquired. A comprehensive description of the XPS measurements is provided in the (Section S1.2.2, Supporting Information).

A quantitative analysis of the core-level HR XPS spectra was carried out using the CasaXPS software (v. 2.3.25PR1.0, Casa Software Ltd.) to determine the relative atomic concertations of constituent elements (Hf, O, N, and C). The N/Hf elemental ratio was calculated using relative atomic concertations for each element. The data fitting and analysis protocols are outlined in the Section S1.2.3 (Supporting Information).

Small Angle X-ray scattering (SAXS, Xeuss 2.0, Xenocs) and X-ray powder diffraction (XRD, SmartLab, Rigaku) diagnostic techniques were used to gather statistically relevant data on the NP size distribution and to gain insight into the NP structure. The 1-D SAXS scattering curves were fitted using the Irena package[71] to obtain the NP number-weighted and volume-weighted size distribution. The structural parameters of the NPs and their oxidation-driven changes were traced by fitting the XRD diffraction patterns using the Rietveld method and MStruct software.[72] A detailed description of measurements with both X-ray diagnostics methods is provided in the (Section S1.2.4, Supporting Information). Additional details on the X-ray diagnostic toolset can be found in previous publication.[65]

The optical spectra of the NPs were obtained by Ultraviolet–Visible-Near–Infrared (UV–Vis–NIR, Cary 7000, Agilent Technologies) spectrophotometric measurements at room temperature (RT, 25 °C) and while the samples were heated in the air up to 800 °C. The steady-state UV–Vis–NIR measurements at RT were carried out at multiple angles using a spectrophotometer (Cary 7000, Agilent Technologies) equipped with the Universal Measurement Accessory (UMA). Multi-angle transmission (T) and reflection (R) spectra were recorded for s and p incident light polarizations, while absorption (A) was calculated as $100 - (T_{total} + R_{total})$. The obtained spectra were compared to those recorded on the same samples, but using a spectrophotometer (Lambda 1050, PerkinElmer Inc.) equipped with an integrating sphere (150 mm in diameter) to evaluate the influence of diffusive scattering. During air annealing, the optical spectra were acquired in transmission geometry using a UV–Vis spectrophotometer (MCS621, Carl Zeiss Spectroscopy GmbH) optically attached to a lab oven via optical fiber waveguides. An average sample heating rate was 16 °C min⁻¹, and transmission spectra were taken every 4 s.

The thicknesses and optical constants of the NP coatings deposited on Si substrates were determined through Spectroscopic Ellipsometry (SE, M2000DI, J. A. Woolam) analysis. Measurements were conducted across the wavelength range from 400 to 1700 nm at three angles: 55°, 65°, and 75°. The ellipsometry data were fitted using CompleteEASE software (J. A. Woollam) employing the Effective Medium Approximation model (EMA, Bruggeman) with three components: HfN,[73] HfO$_2$,[74] and void to represent pores in the coatings. The optimal fit was achieved using a gradient model comprising three layers with a variable void component. The details can be found in the ESI (Section S1.2.5, Supporting Information).

The Ultraviolet Photoelectron Spectroscopy (UPS, ADES-400, V.G. Scientific UK) was employed for the analysis of the HfN NP valence band (VB) structure. The position of the valence band maximum (VBM) was determined as the intersection point between a linear extrapolation of the leading edge of the VB spectrum and the baseline. A more detailed description of the UPS measurements is provided in Section S1.2.6 (Supporting Information).

Finite-Difference Time-Domain Simulations: The experimental measurements were complemented by Finite-Difference Time-Domain (FDTD) simulations using Lumerical software (Ansys, Inc.). These simulations aimed to analyze the absorption and scattering efficiencies of NPs and assess the impact of oxidation, NP size, and interparticle distance on these properties. Furthermore, a simulation of the transmission/reflection/absorption (TRA) spectra of the NP coatings was carried out, utilizing the optical constants (thickness, refractive index, and extinction coefficient) measured through spectroscopic ellipsometry. Additionally, the NP refractive index sensitivity (referred to as the RI sensitivity) and the plasmonic decay length were calculated using the

FDTD model. Detailed descriptions of the models and procedures can be found in the (Section S1.3, Supporting Information).

Supporting Information

Supporting Information is available from the Wiley Online Library or from the author.

Conflict of Interest

The authors declare no conflict of interest.

Data Availability Statement

The data that support the findings of this study are available from the corresponding author upon reasonable request.

[1] R. Zia, J. A. Schuller, A. Chandran, M. L. Brongersma, *Mater. Today* **2006**, *9*, 20.
[2] M. L. Brongersma, V. M. Shalaev, *Science (80-.).* **2010**, *328*, 440.
[3] S. I. Bozhevolnyi, N. A. Mortensen, *Nanophotonics* **2017**, *6*, 1185.
[4] K. M. Mayer, J. H. Hafner, *Chem. Rev.* **2011**, *111*, 3828.
[5] K. A. Willets, A. J. Wilson, V. Sundaresan, P. B. Joshi, *Chem. Rev.* **2017**, *117*, 7538.
[6] W. Park, D. Lu, S. Ahn, *Chem. Soc. Rev.* **2015**, *44*, 2940.
[7] S. I. Azzam, A. V. Kildishev, R. M. Ma, C. Z. Ning, R. Oulton, V. M. Shalaev, M. I. Stockman, J. L. Xu, X. Zhang, *Light Sci. Appl.* **2020**, *9*, 90.
[8] M. L. Brongersma, N. J. Halas, P. Nordlander, *Nat. Nanotechnol.* **2015**, *10*, 25.
[9] S. Inasawa, M. Sugiyama, Y. Yamaguchi, *J. Phys. Chem. B* **2005**, *109*, 3104.
[10] M. A. Asoro, J. Damiano, P. J. Ferreira, *Microsc. Microanal.* **2009**, *15*, 706.

ADVANCED
SCIENCE NEWS

www.advancedsciencenews.com

ADVANCED
OPTICAL
MATERIALS

www.advopticalmat.de

[11] K. Setoura, D. Werner, S. Hashimoto, *J. Phys. Chem. C* **2012**, *116*, 15458.

[12] P. Patsalas, N. Kalfagiannis, S. Kassavetis, G. Abadias, D. V. Bellas, C. Lekka, E. Lidorikis, *Mater. Sci. Eng. R Reports* **2018**, *123*, 1.

[13] D. Steinmüller-Nethl, R. Kovacs, E. Gornik, P. Rödhammer, *Thin Solid Films* **1994**, *237*, 277.

[14] M. Kumar, N. Umezawa, S. Ishii, T. Nagao, *ACS Photonics* **2016**, *3*, 43.

[15] L. Pan, D. B. Bogy, *Nat. Photonics* **2009**, *3*, 189.

[16] W. A. Challener, C. Peng, A. V. Itagi, D. Karns, W. Peng, Y. Peng, X. Yang, X. Zhu, N. J. Gokemeijer, Y.-T. Hsia, G. Ju, R. E. Rottmayer, M. A. Seigler, E. C. Gage, *Nat. Photonics* **2009**, *3*, 220.

[17] X. Wang, X. Wang, Q. Yue, H. Xu, X. Zhong, L. Sun, G. Li, Y. Gong, N. Yang, Z. Wang, Z. Liu, L. Cheng, *Nano Today* **2021**, *39*, 101170.

[18] E. Traver, R. A. Karaballi, Y. E. Monfared, H. Daurie, G. A. Gagnon, M. Dasog, *ACS Appl. Nano Mater.* **2020**, *3*, 2787.

[19] L. Hultman, *Vacuum* **2000**, *57*, 1.

[20] T. Krekeler, S. S. Rout, G. V. Krishnamurthy, M. Störmer, M. Arya, A. Ganguly, D. S. Sutherland, S. I. Bozhevolnyi, M. Ritter, K. Pedersen, A. Y. Petrov, M. Eich, M. Chirumamilla, *Adv. Opt. Mater.* **2021**, *9*, 2100323.

[21] K. Setoura, S. Ito, *AIP Adv.* **2021**, *11*, 115027.

[22] R. A. Karaballi, G. Humagain, B. R. A. Fleischman, M. Dasog, *Angew. Chemie* **2019**, *131*, 3179.

[23] B. T. Diroll, A. Brumberg, A. A. Leonard, S. Panuganti, N. E. Watkins, S. A. Cuthriell, S. M. Harvey, E. D. Kinigstein, J. Yu, X. Zhang, M. G. Kanatzidis, M. R. Wasielewski, L. X. Chen, R. D. Schaller, *Nanoscale* **2021**, *13*, 2658.

[24] M. Parvizian, J. De Roo, *Nanoscale* **2021**, *13*, 18865.

[25] M. Dasog, *Chem. Mater.* **2022**, *34*, 4249.

[26] M. S. Shishodia, P. Pathania, *Phys. Plasmas* **2018**, *25*, 042101.

[27] S. H. C. Askes, N. J. Schilder, E. Zoethout, A. Polman, E. C. Garnett, *Nanoscale* **2019**, *11*, 20252.

[28] S. H. C. Askes, E. C. Garnett, *Adv. Mater.* **2021**, *33*, 2105192.

[29] D. B. O'Neill, S. K. Frehan, K. Zhu, E. Zoethout, G. Mul, E. C. Garnett, A. Huijser, S. H. C. Askes, *Adv. Opt. Mater.* **2021**, *9*, 2100510.

[30] C. V. P. Vital, S. Farooq, R. E. de Araujo, D. Rativa, L. A. Gómez-Malagón, *Appl. Therm. Eng.* **2021**, *190*, 116799.

[31] C. Defilippi, D. V. Shinde, Z. Dang, L. Manna, C. Hardacre, A. J. Greer, C. D'Agostino, C. Giordano, *Angew. Chemie – Int. Ed.* **2019**, *58*, 15464.

[32] P. Pleskunov, T. Košutová, M. Vaidulych, D. Nikitin, Z. Krtouš, S. Ali-Ogly, K. Kishenina, R. Tafiichuk, H. Biederman, I. Gordeev, J. Drewes, I. Barg, F. Faupel, M. Cieslar, R. Yatskiv, Y. Pihosh, V. Nandal, K. Seki, K. Domen, A. Choukourov, *Appl. Surf. Sci.* **2021**, *149974*, *559*.

[33] K. Biliak, M. Protsak, P. Pleskunov, D. Nikitin, J. Hanuš, S. Ali-Ogly, J. Šomvársky, M. Tosca, M. Cieslar, T. Košutová, M. Dopita, F. L. Ferreira, A. Choukourov, *ACS Appl. Nano Mater.* **2023**, *6*, 21642.

[34] M. Protsak, K. Biliak, D. Nikitin, P. Pleskunov, M. Tosca, S. Ali-Ogly, J. Hanuš, L. Hanykova, V. Červenková, A. Sergievskaya, S. Konstantinidis, D. Cornil, J. Cornil, M. Cieslar, T. Košutová, T. Popelář, L. Ondic, A. Choukourov, *Nanoscale* **2024**, *16*, 2452.

[35] L. C. Hernández Mainet, L. P. Cabrera, E. Rodriguez, A. F. Cruz, G. Santana, J. L. Menchaca, E. Pérez-Tijerina, *Nanoscale Res. Lett.* **2012**, *7*, 80.

[36] A. Reinholdt, R. Detemple, A. L. Stepanov, T. E. Weirich, U. Kreibig, *Appl. Phys. B* **2003**, *77*, 681.

[37] A. Reinholdt, R. Pecenka, A. Pinchuk, S. Runte, A. L. Stepanov, T. E. Weirich, U. Kreibig, *Eur. Phys. J. D – At. Mol. Opt. Plasma Phys.* **2004**, *31*, 69.

[38] H. Sugimoto, S. Ikuno, M. Fujii, *ACS Appl. Nano Mater* **2019**, *2*, 6769.

[39] A. Alvarez Barragan, N. V. Ilawe, L. Zhong, B. M. Wong, L. Mangolini, *J. Phys. Chem. C* **2017**, *121*, 2316.

[40] S. Exarhos, A. Alvarez-Barragan, E. Aytan, A. A. Balandin, L. Mangolini, *ACS Energy Lett.* **2018**, *3*, 2349.

[41] I. Hotový, J. Huran, D. Búc, R. Srnánek, *Vacuum* **1998**, *50*, 45.

[42] H. Nowotny, F. Benesovsky, E. Rudy, *Monatshefte für Chemie und verwandte Teile anderer Wissenschaften* **1960**, *91*, 348.

[43] V. N. Popok, I. Barke, E. E. B. Campbell, K.-H. Meiwes-Broer, *Surf. Sci. Rep.* **2011**, *66*, 347.

[44] L. Mädler, A. A. Lall, S. K. Friedlander, *Nanotechnology* **2006**, *17*, 4783.

[45] F. Borghi, M. Milani, L. G. Bettini, A. Podestà, P. Milani, *Appl. Surf. Sci.* **2019**, *479*, 395.

[46] J. A. Scholl, A. L. Koh, J. A. Dionne, *Nature* **2012**, *483*, 421.

[47] X. Fan, W. Zheng, D. J. Singh, *Light Sci. Appl.* **2014**, *3*, e179.

[48] R. A. Karaballi, Y. E. Monfared, M. Dasog, *Langmuir* **2020**, *36*, 5058.

[49] S. Chung, S. Shrestha, X. Wen, Y. Feng, N. Gupta, H. Xia, P. Yu, J. Tang, G. Conibeer, *Sol. Energy Mater. Sol. Cells* **2016**, *144*, 781.

[50] HOYA Group Optics Division, Colored Glass Filters: Green Filters (G), https://www.hoyacandeo.co.jp/english/products/eo/color/05.html (accessed: October 2023).

[51] M. Honda, Y. Saito, S. Kawata, *Appl. Phys. Express* **2014**, *7*, 112402.

[52] S. K. Ghosh, T. Pal, *Chem. Rev.* **2007**, *107*, 4797.

[53] A. M. Funston, C. Novo, T. J. Davis, P. Mulvaney, *Nano Lett.* **2009**, *9*, 1651.

[54] A. Movsesyan, A. Muravitskaya, M. Castilla, S. Kostcheev, J. Proust, J. Plain, A.-L. Baudrion, R. Vincent, P.-M. Adam, *J. Phys. Chem. C* **2021**, *125*, 724.

[55] E. Prodan, P. Nordlander, *J. Chem. Phys.* **2004**, *120*, 5444.

[56] P. Muñoz, G. Micó, L. A. Bru, D. Pastor, D. Pérez, J. D. Doménech, J. Fernández, R. Baños, B. Gargallo, R. Alemany, A. M. Sánchez, J. M. Cirera, R. Mas, C. Domínguez, *Sensors* **2017**, *17*, 2088.

[57] X. Wu, Y. Kodera, J. E. Garay, *Mater. Des.* **2022**, *223*, 111177.

[58] J. N. Anker, W. P. Hall, O. Lyandres, N. C. Shah, J. Zhao, R. P. Van Duyne, *Nat. Mater.* **2008**, *7*, 442.

[59] M. E. Stewart, C. R. Anderton, L. B. Thompson, J. Maria, S. K. Gray, J. A. Rogers, R. G. Nuzzo, *Chem. Rev.* **2008**, *108*, 494.

[60] L. S. Jung, C. T. Campbell, T. M. Chinowsky, M. N. Mar, S. S. Yee, *Langmuir* **1998**, *14*, 5636.

[61] A. J. Haes, R. P. Van Duyne, *J. Am. Chem. Soc.* **2002**, *124*, 10596.

[62] T. Lednický, A. Bonyár, *ACS Appl. Mater. Interfaces* **2020**, *12*, 4804.

[63] L. Gan, M. Heggen, C. Cui, P. Strasser, *ACS Catal.* **2016**, *6*, 692.

[64] T. S. Sakthivel, D. L. Reid, U. M. Bhatta, G. Möbus, D. C. Sayle, S. Seal, *Nanoscale* **2015**, *7*, 5169.

[65] T. Košutová, L. Horák, P. Pleskunov, J. Hanuš, D. Nikitin, P. Kúš, M. Cieslar, I. Gordeev, S. Burazer, A. Choukourov, M. Dopita, *Mater. Chem. Phys.* **2022**, *277*, 125466.

[66] J. Kousal, A. Shelemin, M. Schwartzkopf, O. Polonskyi, J. Hanuš, P. Solař, M. Vaidulych, D. Nikitin, P. Pleskunov, Z. Krtouš, T. Strunskus, F. Faupel, S. V. Roth, H. Biederman, A. Choukourov, *Nanoscale* **2018**, *10*, 18275.

[67] A. Shelemin, P. Pleskunov, J. Kousal, J. Drewes, J. Hanuš, S. Ali-Ogly, D. Nikitin, P. Solař, J. Kratochvíl, M. Vaidulych, M. Schwartzkopf, O. Kylián, O. Polonskyi, T. Strunskus, F. Faupel, S. V. Roth, H. Biederman, A. Choukourov, *Part. Part. Syst. Charact.* **2020**, *37*, 1900436.

[68] A. Choukourov, D. Nikitin, P. Pleskunov, R. Tafiichuk, K. Biliak, M. Protsak, K. Kishenina, J. Hanuš, M. Dopita, M. Cieslar, T. Popelář, L. Ondič, M. Varga, *J. Mol. Liq.* **2021**, *336*, 116319.

[69] K. Biliak, D. Nikitin, S. Ali-Ogly, M. Protsak, P. Pleskunov, M. Tosca, A. Sergievskaya, D. Cornil, J. Cornil, S. Konstantinidis, T. Košutová, Z. Černochová, P. Štěpánek, J. Hanuš, J. Kousal, L. Hanyková, I. Krakovský, A. Choukourov, *Nanoscale Adv* **2023**, *5*, 955.

[70] P. Pleskunov, T. Košutová, M. Protsak, M. Tosca, K. Biliak, D. Nikitin, Z. Krtouš, J. Hanuš, J. Houška, M. Cieslar, S. Ali-Ogly, P. Kúš, O. Kylián, A. Choukourov, *Appl. Surf. Sci.* **2023**, *639*, 158235.

[71] J. Ilavsky, P. R. Jemian, *J. Appl. Crystallogr.* **2009**, *42*, 347.

[72] Z. Matěj, R. Kužel, L. Nichtová, *Powder Diffr.* **2010**, *25*, 125.

[73] E. D. Palik, *Handbook of Optical Constants of Solids*, Academic Press, Boston, MA, **1997**.

[74] T. J. Bright, J. I. Watjen, Z. M. Zhang, C. Muratore, A. A. Voevodin, *Thin Solid Films* **2012**, *520*, 6793.